lubricants

MDPI

Article

An Experimental Study on the Fretting Corrosion Behaviours of Three Material Pairs at Modular Interfaces for Hip Joint Implants

Jian Pu [1], Dongsheng Wu [1], Yali Zhang [1,*], Xiaogang Zhang [1] and Zhongmin Jin [1,2,*]

[1] Tribology Research Institute, School of Mechanical Engineering, Southwest Jiaotong University, Chengdu 610031, China; pu1995@my.swjtu.edu.cn (J.P.); wdsgogogo@163.com (D.W.); xg@swjtu.edu.cn (X.Z.)
[2] School of Mechanical Engineering, University of Leeds, Leeds LS2 9JT, UK
* Correspondence: zhangyali@swjtu.edu.cn (Y.Z.); zmjin@swjtu.edu.cn (Z.J.)

Abstract: The fretting corrosion behaviours of Al_2O_3 ceramic/Ti6Al4V alloy, 316 L stainless/Ti6Al4V alloy, and CoCrMo alloy/Ti6Al4V alloy pairs were studied in an in-house developed fretting-corrosion tester. The fretting behaviours were characterized by the F_t-D-N and F_t/F_n curves. The morphology of the worn surface was analyzed by energy dispersive X-ray spectrometry (EDX), a scanning electron microscope (SEM), and a white light interferometer (WLI). The fretting regimes were found to vary from slip regime (SR) to mixed fretting regime (MFR), with an increase in loads for the Al_2O_3/Ti6Al4V and 316 L/Ti6Al4V pairs, while for the CoCrMo/Ti6Al4V pair the fretting always remained in SR. The damage mechanism of the Al_2O_3/Ti6Al4V pair was mainly abrasive wear and corrosive wear, while for the 316 L/Ti6Al4V pair and CoCrMo/Ti6Al4V pair, the wear mechanism was mainly adhesive wear and corrosive wear with slight abrasive wear. The electrochemical impedance spectrum results show that the material transfer layer formed on the surface of the material can protect the material from corrosion for the 316 L/Ti6Al4V and CoCrMo/Ti6Al4V pairs.

Keywords: Ti6Al4V; fretting corrosion; wear mechanism; abrasive wear; adhesive wear

Citation: Pu, J.; Wu, D.; Zhang, Y.; Zhang, X.; Jin, Z. An Experimental Study on the Fretting Corrosion Behaviours of Three Material Pairs at Modular Interfaces for Hip Joint Implants. *Lubricants* **2021**, *9*, 12. https://doi.org/10.3390/lubricants9020012

Received: 14 December 2020
Accepted: 19 January 2021
Published: 21 January 2021

1. Introduction

Artificial joint implantation is used to treat joint diseases and trauma and is one of the most successful surgical treatments in the field of orthopedics [1]. At present, artificial hip joints have evolved from a monoblock design to the popular modular design, which enables the head and stem of the implant to use different materials [2]. Also, the modular design allows surgeons to match the most appropriate configurations for each patient to achieve better outcomes [3,4]. However, the combined head–neck interface and neck-stem interface introduced by the modular design also brings some clinical problems. A fastening contact interface is formed between two connecting parts, such as the head and neck. Under daily activities of the human body, there is a cyclic relative motion of small amplitude (micromovement as shown in Figure 1) between the contact interface. Finite element studies have shown that the micro-motion of the head–neck position in daily activities ranges from 0 to 38 μm [5,6]. At the same time, as body fluid enters the gap between the two contact surfaces, a corrosive environment is formed. The coupling of micromotion and corrosion results in fretting corrosion. Fretting corrosion is a chemical-mechanical process that could cause serious material damage [7–10]. It is well known that there is widespread fretting corrosion in the conical connection of the ball head and the femoral stem in total hip joints [11–20]. Similar phenomena also exist in the knee joints, shoulder joints, and spinal fixation that use the modular assembly [21–27].

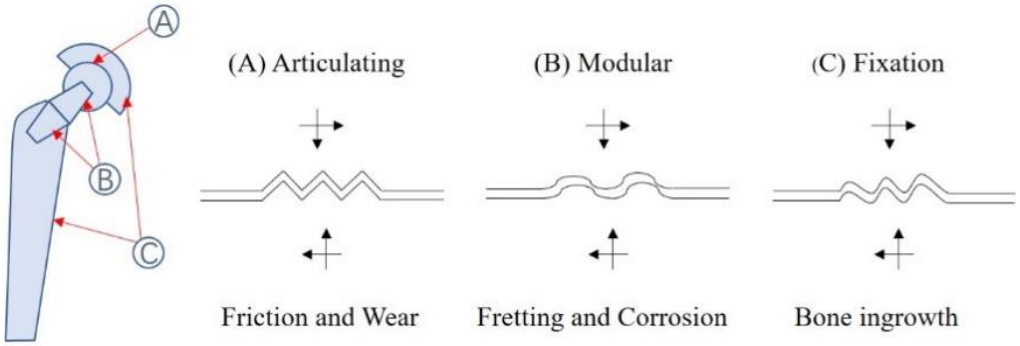

Figure 1. Damage mechanism of the contact interfaces in an artificial hip joint.

In the past decades, the fretting corrosion behaviours of materials used for artificial joints have been investigated in many studies on the effects of mechanical conditions such as load, frequency, and displacement amplitude as well as electrochemical conditions such as pH, potential, and corrosive media. Swaminathan and Gilbert [28] and Royhman et al. [29] proposed a basic model for fretting corrosion experiments. For a given material pair in an electrochemical environment, a single fretting mode and different pH values were applied to measure the fretting current, friction coefficient/friction dissipation energy, etc. Barril et al. [30,31] studied the fretting corrosion behaviour of titanium alloys under different load and displacement amplitudes, pointing out that there was only significant wear in the slip zone. Royhman et al. [29,32,33] confirmed that the fretting friction coefficient and dissipation energy were affected by potential and solution chemistry. Liu et al. [34] found that the presence of inflammatory factors in the body reduced the stability of the oxide film on the surface of the alloy. In addition, torsional fretting corrosion behaviours of materials for artificial joints were also studied by Wang [35,36] and Lin [37,38].

At present, the material combinations used for artificial joints are mainly cobalt chromium molybdenum alloy, titanium alloy, stainless steel, and ceramic materials, with a number of variations. Clinical studies have shown that the corrosion behaviours at the joint interface of the hip joint are closely related to the material combinations, where galvanic corrosion may occur at the joint of different metal materials due to the difference of electric potential [17,39,40]. However, most researchers carried out experimental studies on one or two kinds of material combinations, therefore lacking a systematic comparison and sufficient understanding of fretting corrosion behaviours under various head and neck combinations. Therefore, the fretting corrosion behaviours of three typical material combinations of Al_2O_3/Ti6Al4V, 316 L/Ti6Al4V, and CoCrMo/Ti6Al4V were investigated in a new multifunctional fretting test machine in this paper, and the effects of contact load were also considered.

2. Materials and Methods

2.1. Materials

A ball/plane model was adopted in this study. The plane was made of a medical-grade Ti6Al4V for three pairs. There were three kinds of materials for the ball specimen—Al_2O_3 ceramic, 316 L stainless, and CoCrMo alloy—with a diameter of 12 mm. The chemical composition and main mechanical properties of the above four materials are shown in Tables 1–5. Thus, three material combinations, Al_2O_3/Ti6Al4V, 316 L/Ti6Al4V, and CoCrMo/Ti6Al4V, were compared in this study. Ti6Al4V was cut into 10 mm × 10 mm × 5 mm blocks by wire cutting. The surface was ground with 400 mesh, 600 mesh, and 800 mesh sandpapers to simulate the real head and neck surface roughness. Then, the sample was ultrasonically cleaned in absolute ethanol for 10 min, and finally dried and stored. Wires were soldered to the bottom of the block and inlaid with a metallographic insert, leaving only a 10 mm × 10 mm plane in contact.

Table 1. Chemical composition (wt. %) of Ti6Al4V alloy.

Elements	Al	V	Fe	C	O	N	H	Ti
Percentage	6.05 ± 0.63	3.95 ± 0.5	0.11	0.014	0.140	0.006	0.001	Balance

Table 2. Chemical composition (wt. %) of CoCrMo alloy.

Elements	Cr	Mo	Ni	Fe	Mn	Si	C	N	Co
percentage	28.10 ± 2.10	5.90 ± 1.10	0.88	0.65	0.63	0.22	0.25	0.12	Balance

Table 3. Chemical composition (wt. %) of 316 L alloy.

Elements	Cr	Ni	Mo	Mn	Si	Co	C	Cu	S	Fe
Percentage	17.4 ± 1.6	13.0 ± 0.7	2.6 ± 0.4	1.73 ± 0.6	0.66	0.20	0.0165	0.097	<0.001	Balance

Table 4. Chemical composition (wt. %) of Al_2O_3 ceramic.

Elements	Al_2O_3	Na_2O	CaO	SiO_2	Magnetic
Percentage	≥98.5	≤0.5	≤0.5	≤0.3	≤0.003

Table 5. Main mechanical properties of Al_2O_3 ceramic, 316 L steel, CoCrMo alloy, and Ti6Al4V alloy.

Materials	Tensile Strength (MPa)	Yield Strength (MPa)	Elongation (%)	Elastic Modulus (GPa)	Poisson's Ratio	Hardness (HV)
Al_2O_3 ceramic	/	/	/	370	0.2	1500
316 L steel	635	280	12	197	0.3	150
CoCrMo alloy	1507	962	20	200	0.3	320
Ti6Al4V alloy	860	795	12	110	0.3	260

2.2. Methods and Devices

In the current study, an in-house multi-function fretting-corrosion test apparatus (MFC-01) was developed. As shown in Figure 2, the apparatus consisted of a fretting module and an electrochemical workstation (CHI660E, Chenhua, China). For the fretting module, the normal load was achieved by shaking the feed motion of the hand-wheel ball screw pair to drive the slider down to compress the spring, and the tangential displacement was achieved by a piezoelectric ceramic driver. The upper clamp was insulated to avoid interference with the electrochemical signal. The block sample was installed in the lower clamp and connected to the working electrode of the workstation through a wire. A three-electrode system was used in the electrochemical test: the sample as the working electrode, a platinum plat with an area of 1 cm^2 as the counter electrode, and Ag/AgCl (saturated potassium chloride) as the reference electrode.

The fretting tests were conducted under a series of loads (F_n) of 5, 10, and 15 N. The frequency (f) and the displacement amplitude (D) for all tests were 1 Hz and 10 μm, respectively. The fretting number of cycles (N) was 6000, and the test duration was 6000 s. The experimental medium was a saline solution with a volume fraction of 10% bovine serum. When fretting was over, electrochemical impedance spectroscopy measurement with a frequency of 10^5–10^{-2} Hz and an AC signal amplitude of 10 mV was performed immediately. All tests were performed at a room temperature of 25 ± 3 °C and repeated at least three times. The detailed test parameters are listed in Table 6.

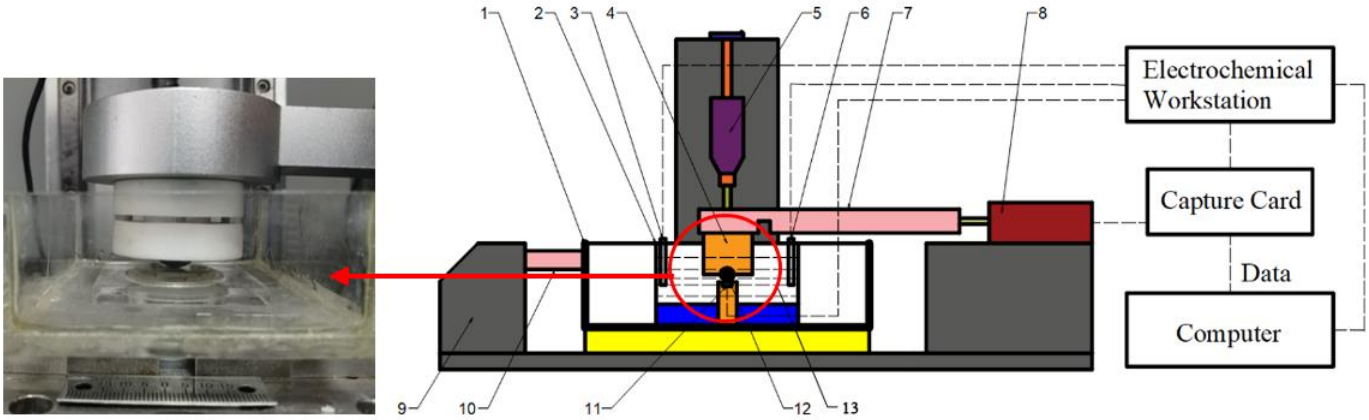

Figure 2. Simplified diagram of the fretting-corrosion device. 1: stage, 2: electrolyte container, 3: counter electrode, 4: upper clamp, 5: load sensor, 6: reference electrode, 7: connecting rod, 8: piezoelectric ceramic, 9: shockproof table, 10: bracket, 11: upper sample, 12: lower sample, and 13: electrolyte solution.

Table 6. Fretting corrosion test parameters.

Parameter	Values
Displacement, D	D = 10 μm
Normal load, F_N	$F_{N,1}$ = 5 N; $F_{N,2}$ = 10 N; $F_{N,3}$ = 15 N
Frequency	1 Hz
Test medium	physiological saline with 10% volume bovine serum (100 mL)

The morphologies of the damaged scars were tested using scanning electron microscopy (JSM-6610LV, JEOL, AKISHIMA-SHI, Japan). The chemical composition of the debris was analyzed using energy-dispersive X-ray spectroscopy. The 3D morphology of the worn surface and wear volume was measured using a white light interferometer (GT X3, Bruker, Hanau, Germany).

3. Results and Discussion

3.1. Fretting Running Characteristics

The friction force-displacement (F_t-D) diagram is a reflection of the dynamic characteristics of the fretting interface. According to the different dynamic characteristics of the interface, the fretting behaviours could be divided into three fretting regimes: slip regime (SR), partial slip regime (PSR), and mixed fretting regime (MFR). F_t-D-N curves of three different material pairs under different loads are shown in Figure 3. For all material pairs, the F_t-D diagrams reached a stable state after 100 cycles, indicating that the surface had established an equilibrium contact state at this time. When the load was 5 N, with an increase in cycle numbers, the F_t-D curve was a parallelogram, and the fretting was in SR. When the load was 10 N, the F_t-D diagrams of the three types of mating pairs were still parallelograms in SR. However, when the load was increased to 15 N, for the Al_2O_3/Ti6Al4V and 316 L/Ti6Al4V pairs, the shape of the F_t-D curve gradually changed from a parallelogram to an ellipse shape, indicating that the fretting regime changed from SR to MFR. While the CoCrMo/Ti6Al4V pair showed different trends under this load, the F_t-D diagram was still a parallelogram and the fretting was always in SR. Therefore, compared with the CoCrMo/Ti6Al4V combination, Al_2O_3/Ti6Al4V and 316 L/Ti6Al4V combinations were not easier to slip.

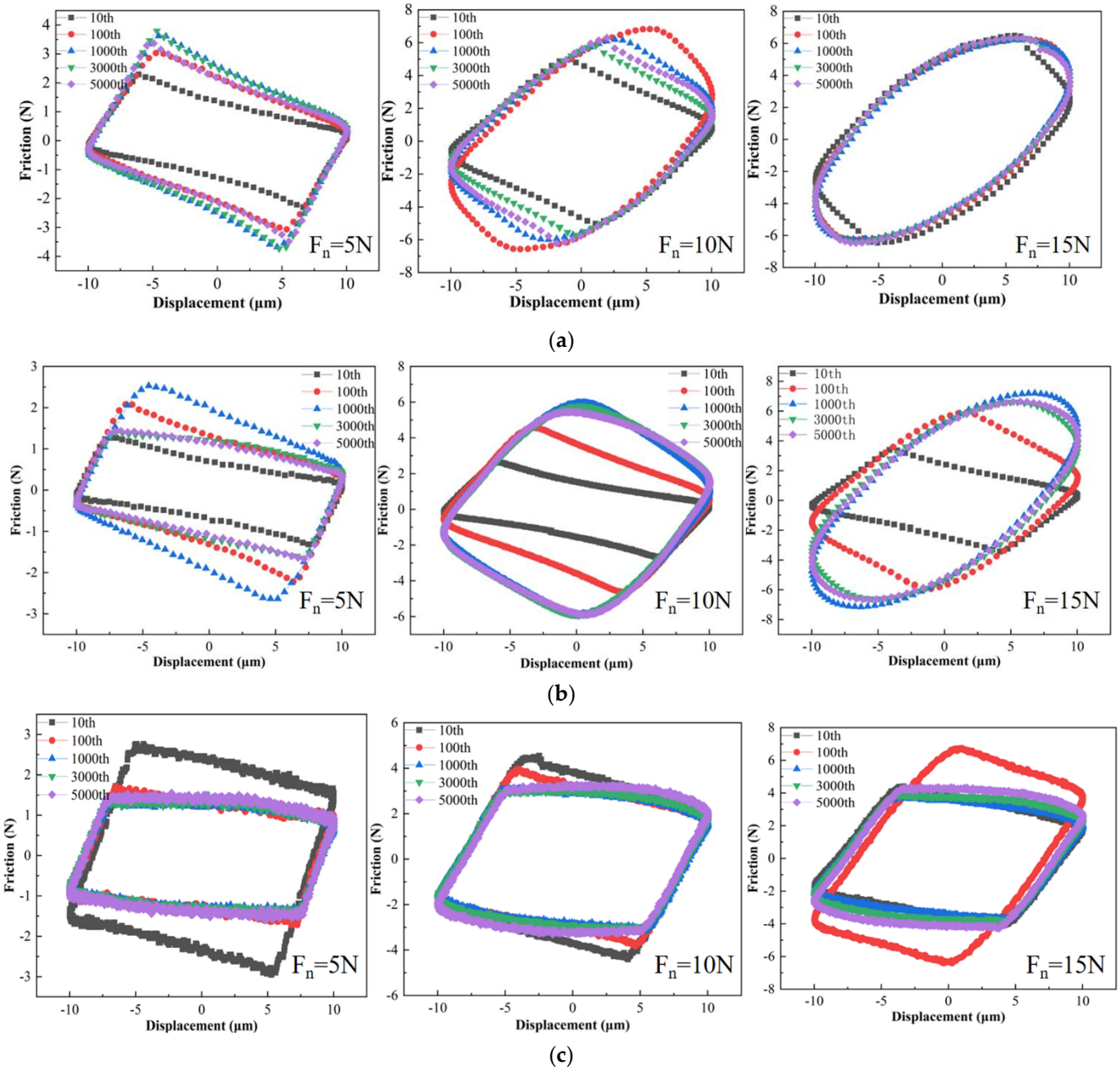

Figure 3. F_t-*D*-*N* diagrams of three material pairs with different loads under different cycles. (**a**) Al_2O_3/Ti6Al4V; (**b**) 316 L/Ti6Al4V; (**c**) CoCrMo/Ti6Al4V.

Dissipated energy is a useful indicator for evaluating fretting damage, which corresponds to the area of the fretting loop. Total energy dissipation is equal to the sum of dissipated energy of each cycle [41,42]. In this study, we calculated the energy dissipation every 100 cycles to reduce the amount of computation. Total energy dissipation for different tribological pairs and loads is depicted in Figure 4. It could be seen that for all loads the total energy dissipation of the Al_2O_3/Ti6Al4V pair was the largest, that of the 316 L/Ti6Al4V pair was medium, and that of the CoCrMo/Ti6Al4V pair was the smallest. According to Sections 3.2 and 3.3, for the Al_2O_3/Ti6Al4V pair, Al_2O_3 ceramic had high hardness and produced a large shear force, which caused a large number of spalling and ploughing marks on the surface of the material. This process consumed a lot of dissipated energy. While for the 316 L/Ti6Al4V pair and CoCrMo/Ti6Al4V pair, the damage of material was mainly adhesion and plastic deformation, which consumed less energy [42].

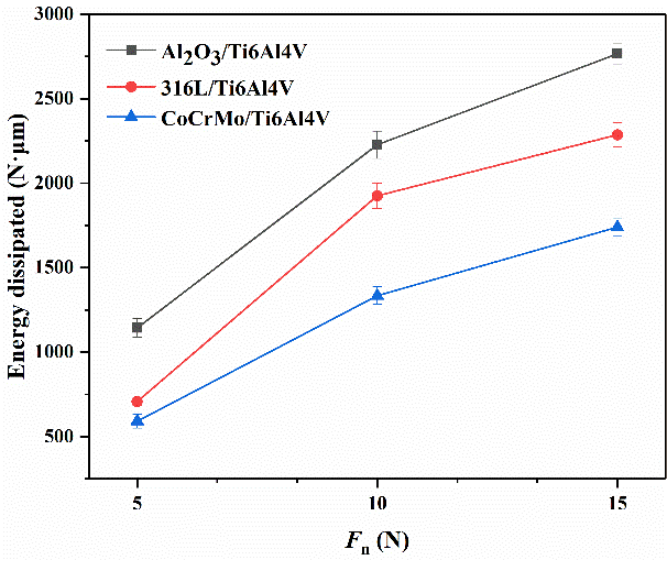

Figure 4. Variation of the total energy dissipated under load for different pairs.

3.2. Analysis of Friction Coefficient

The coefficient of friction is an important index to characterize friction and wear behaviours. The friction coefficient is commonly characterized by the ratio of the average tangential force to the normal load in each circle. Figure 5 compares the coefficients of the three material pairs under different loads. As shown in Figure 5a, with the increase in loads, the coefficients of the Al_2O_3/Ti6Al4V pair showed a downward trend. The fluctuation of the coefficients under 5 N and 10 N was obviously higher than that under 15 N, which was mainly due to the fact that 5 N and 10 N fretting was in SR, and the material peeling and wear were more serious. For the 316 L/Ti6Al4V pair, the friction coefficient and its fluctuation increased with the increase in the loads. The 316 L material had lower elastic modulus and hardness, which made adhesion easier to occur. As the load increased, material transfer and adhesion became more serious during the fretting process, which led to an increase in the friction coefficient and the fluctuation of the coefficient. For the CoCrMo/Ti6Al4V pair, the evolution of coefficient under all loads was similar, indicating that the contact state was similar. The coefficients decreased with the increase in loads, revealing that the debris layer had a role in reducing friction and lubrication.

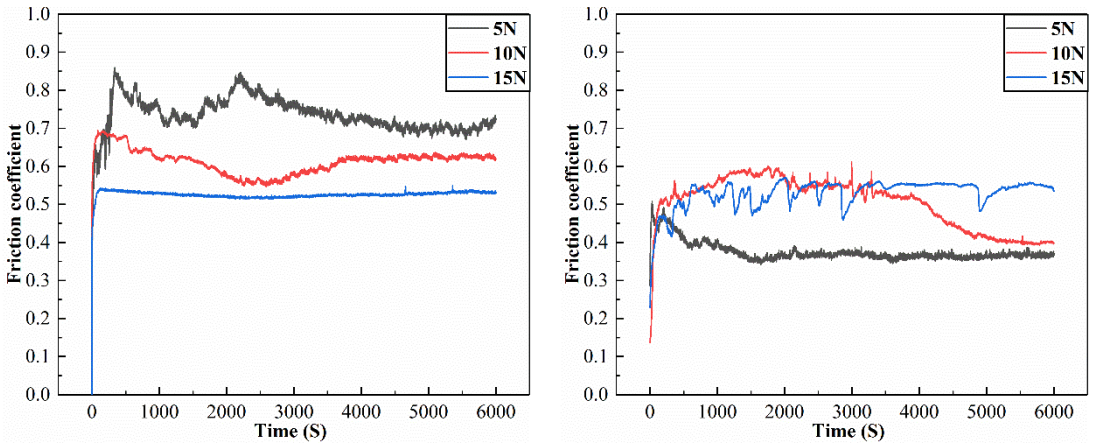

Figure 5. *Cont.*

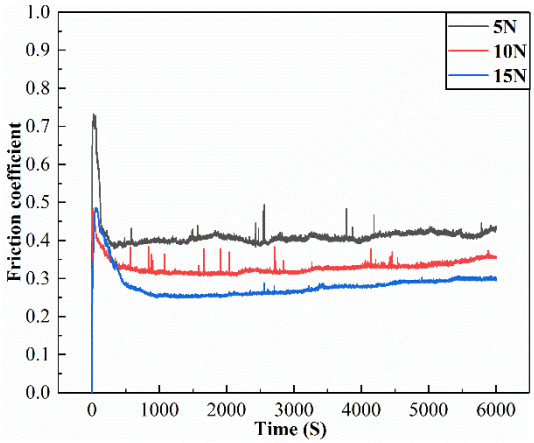

(**c**)

Figure 5. Variation of friction coefficient of three types of pairing under different loads. (**a**) Al_2O_3/Ti6Al4V; (**b**) 316L/Ti6Al4V; (**c**) CoCrMo/Ti6Al4V.

3.3. Analysis of Wear Morphology

To understand the damage mechanism of Ti6Al4V alloy under different pairs, the morphology of the wear scar of Ti6Al4V alloy under different pairs was obtained as shown in Figures 6–8. In addition, the two-dimensional profile and EDX spectra of the wear marks under some conditions were also measured, which are exhibited in Tables 7–9.

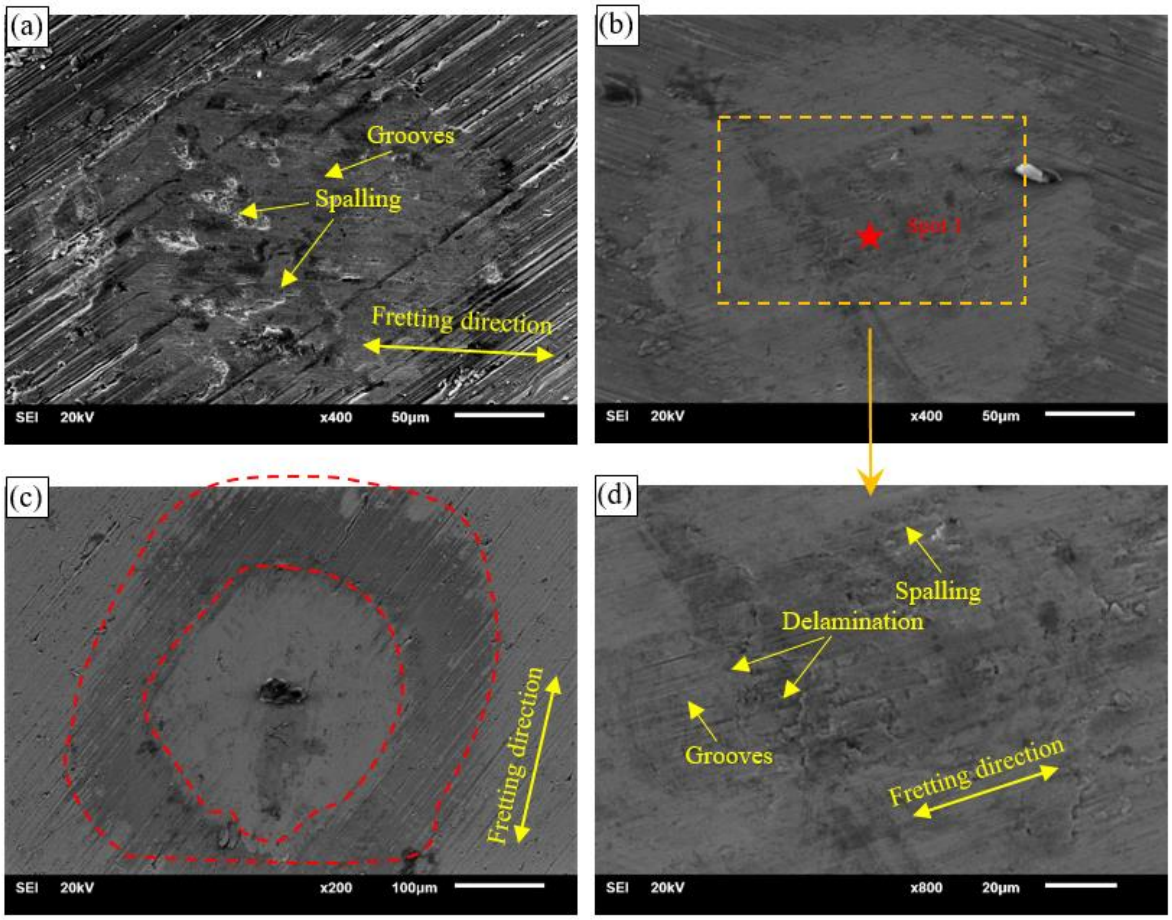

Figure 6. SEM micrographs of the wear scars of Ti6Al4V alloy for the Al_2O_3-Ti6Al4V pair under various loads. (**a**) 5 N; (**b**) 10 N; (**c**) 15 N; (**d**) enlarged view of the area marked by the dashed box in (**b**).

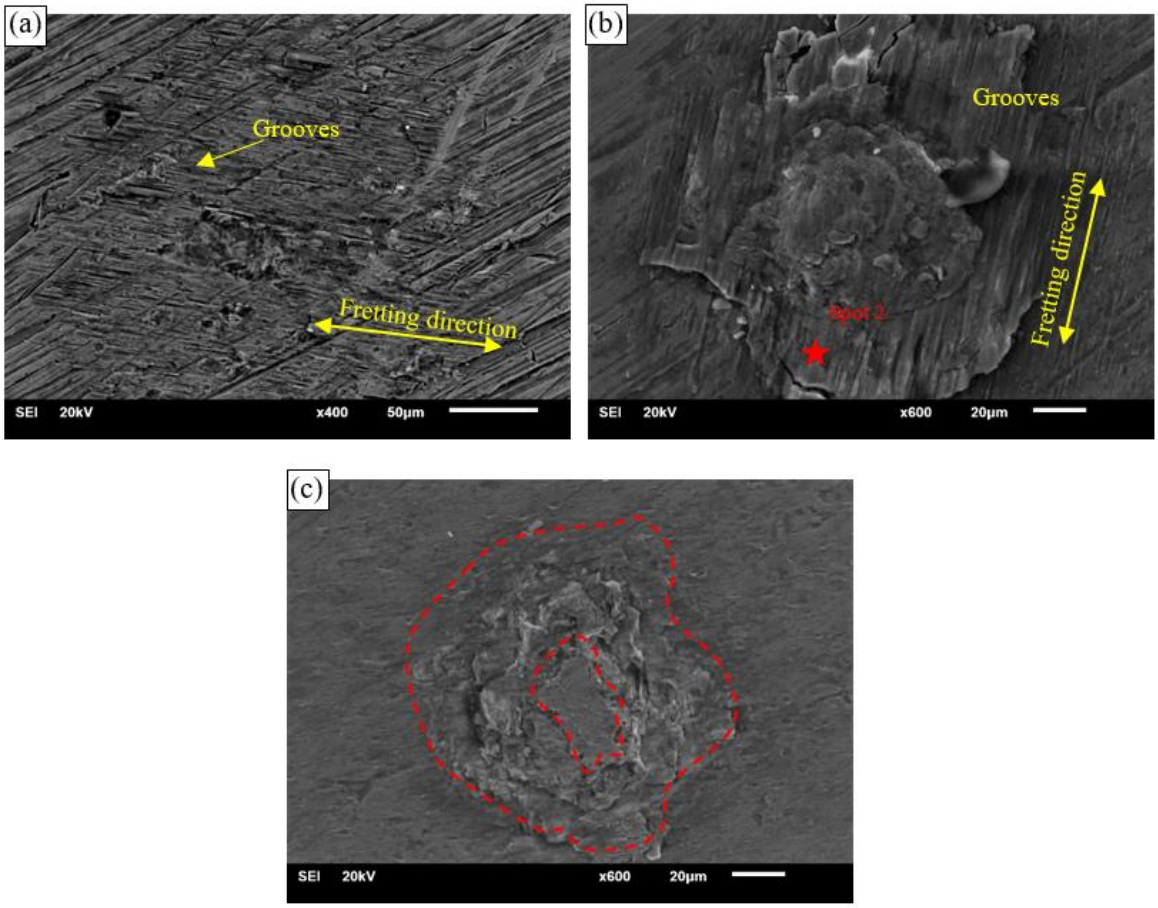

Figure 7. SEM micrographs of wear scars of Ti6Al4V alloy for the 316 L/Ti6Al4V pair under various loads. (**a**) 5 N; (**b**) 10 N; (**c**) 15 N.

Table 7. EDX analysis of spot 1 in Figure 6 (The error is about 2%).

Element	O	Al	Si	Cl	Ti	V
Wt.%	27.31	3.72	0.53	0.19	65.91	2.34

Table 8. EDX analysis of spot 2 in Figure 7 (The error is about 2%).

Element	C	O	Na	Al	Si	Cl	K	Ti	V	Cr	Fe	Ni	Cu
Wt.%	4.14	45.4	0.65	0.19	0.59	2.7	0.34	4.52	0.3	25.11	11.32	3.66	1.07

Table 9. EDX analysis of spot 3 in Figure 8 (The error is about 2%).

Element	C	O	Na	Al	Cl	K	Ca	Ti	V	Cr	Co	Mo
Wt.%	1.62	50.62	0.60	0.71	0.96	0.41	0.16	20.14	1.13	16.95	3.53	3.18

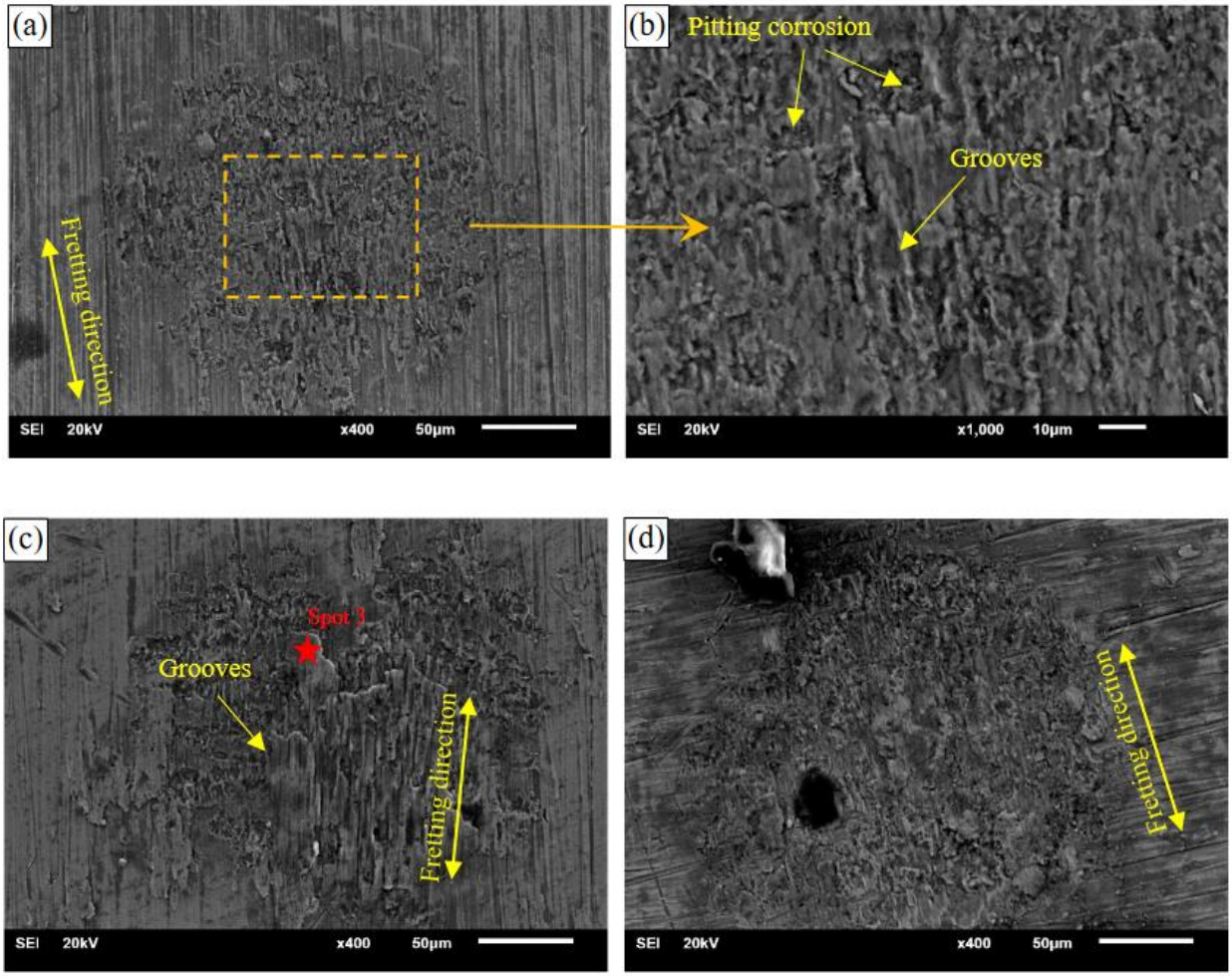

Figure 8. SEM micrographs of wear scars of Ti6Al4V alloy for the Al_2O_3-Ti6Al4V pair under various loads. (**a**) 5 N; (**b**) enlarged view of the area marked by the dashed box in (**a**); (**c**) 10 N; (**d**) 15 N.

Figure 6 is a scanning electron micrograph of the wear scar of Ti6Al4V alloy of the Al_2O_3/Ti6Al4V pair under different loads. It could be seen that when the load was 5 N and 10 N the morphology of wear marks of the Al_2O_3/Ti6Al4V pair presented a typical characteristic of abrasive wear. There were many furrows and spalling pits on the surface of the material, and spalling pits were obviously oxidized. Wear debris could hardly be found on the wear marks, and the main elements of the wear area were Ti, V, and Al (see Table 7), which were the main components of titanium alloy, indicating that material transfer had not occurred. When the load was 15 N, fretting ran in MFR, and the worn surfaces could be divided into a mild sticking area in the center and severe wear areas at the edge. There was no obvious damage observed in the central sticking area, and the damage in the outer wear area was also very slight, showing slight abrasive wear. Therefore, for the Al_2O_3/Ti6Al4V pair, its wear mechanisms were mainly abrasive wear and corrosive wear.

As shown in Figure 7, for the 316 L/Ti6Al4V pair, when the load was 5 N, the wear of the material was slight and the surface of the material was covered with shallow furrows evenly, indicating that abrasive wear was dominant. When the load increased to 10 N, a thick layer of debris was formed on the worn surface, and many grooves parallel to the fretting direction were evenly distributed on the wear debris layer, revealing abrasive wear. Figure 9 shows the existence of the debris bed. The two-dimensional profiles of the two pairs were higher than the surface of the substrate material, which indicated that there was debris accumulation. To clarify the composition of the debris bed, EDX analysis was performed. As illustrated in Table 8, many Fe, Cr, and Ni elements were detected, and these elements were the main constituent elements of 316 L. In addition, the oxygen element

weight percentage reached 45.40%. Because the hardnesses of Ti6Al4V alloy and 316 L stainless steel are similar, it is easy to produce an adhesion effect. Under the action of normal pressure and friction heat, the contact interface adhered. When the fretting started, the adhesive node was sheared and fractured under the action of the tangential force. At this time, the material on the 316 L ball was transferred to the surface of the titanium alloy, and it was repeatedly rolled and oxidized to form a material transfer layer. Thus, its wear mechanisms were mainly adhesive wear, abrasive wear, and corrosive wear. When the load was 15 N, the adhesion effect was strengthened, and fretting ran in MFR. The wear area could be divided into the adhesion area in the middle and the serious wear area at the edge. As the micro slip only occurred at the edge of the contact area, the damage in the middle of the contact area was very slight, and the damage mechanism of the severe wear area at the edge was also adhesive wear, abrasive wear, and corrosive wear.

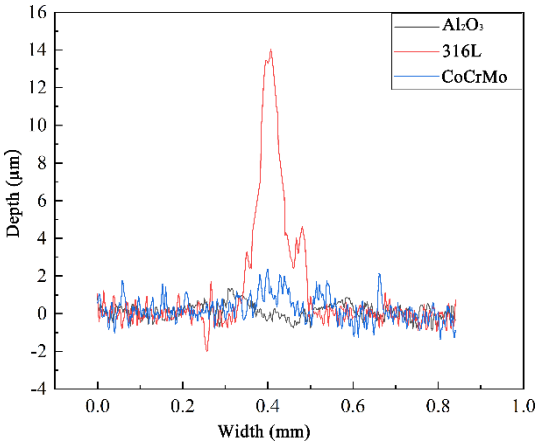

Figure 9. The profile curve of the three material combinations.

Figure 8 is a scanning electron micrograph of the wear scar of Ti6Al4V alloy of the CoCrMo/Ti6Al4V pair under different loads. For all given loads, fretting ran in SR, and the surface of the Ti6Al4V alloy was covered with a debris layer. According to the EDX analysis (see Table 9) and 2D profile (see Figure 9), the existence of the debris layer was confirmed, and its composition contained a large number of elements of CoCrMo. The formation process of the debris layer of the friction pair was similar to the 316 L/Ti6Al4V pair. The damaged area of the material increased with an increase in loads. It could be seen that, for all conditions, grooves were formed on the surface of the material due to ploughing, and a lot of evidence of pitting corrosion could be found. In short, the damage mechanisms for the CoCrMo/Ti6Al4V pair were mainly adhesive wear, abrasive wear, and corrosive wear.

In summary, due to the material properties of the three friction balls, the damage mechanisms of Ti6Al4V alloy under different material combinations were different. The hardness of the Al_2O_3 ceramic ball was as high as 1500 HV, while the base material of Ti6Al4V alloy was only 260 HV. It could directly shear and plough the base material during friction, and the damage mechanism was mainly abrasive wear and corrosive wear. However, the hardness of 316 L alloy and CoCrMo alloy was relatively small, which was 150 HV and 320 HV, respectively. In the process of fretting, the friction interface was easy to adhere to. Therefore, for the 316 L/Ti6Al4V pair, under low load, the adhesion was not obvious, and the damage mechanisms were abrasive wear and corrosive wear. While under high load, the damage mechanisms were adhesive wear and corrosive wear. For the CoCrMo/Ti6Al4V pair, the damage mechanisms were mainly adhesive wear and corrosive wear with slight abrasive wear.

3.4. Electrochemical Impedance Spectrum Analysis

As shown in Section 3.3, we found that after fretting, for the 316 L/Ti6Al4V and CoCrMo/Ti6Al4V pairs, a thick material transfer layer was formed on the surface of the Ti6Al4V alloy, but not for the Al_2O_3/Ti6Al4V pair. In order to determine the effect of the material transfer layer on the corrosion performance of the material, the electrochemical impedance test was carried out on the Ti6Al4V alloy after fretting under three pairs. It should be noted that in electrochemical impedance spectroscopy (EIS) measurement, the tested object is the worn Ti6Al4V alloy itself, and it is not matched with other materials. Figure 10a,b show the Nyquist diagrams of the electrochemical impedance spectroscopy and the Bode diagram, respectively. Figure 11 is an equivalent circuit diagram of an impedance spectrum. The circuit included a solution resistance, R_s, a constant phase element, CPE, a surface film resistance, R_{film}. For three material pairs, Nyquist diagrams all presented an approximate semicircle, indicating that the electrode reaction on the surface of the substrate was mainly controlled by the charge transfer process, and the radius of the semicircle from large to small was the sample after rubbing with 316 L, the sample after rubbing with CoCrMo, and the sample after rubbing with Al_2O_3. The Bode diagram shows that the substrate electrode reaction system under the three material pairs had only one time constant, and the phase angle peak under the Al2O3/Ti6Al4V pair had the lowest peak width and the narrowest peak width, indicating that the damage to surface film was more serious than the other two pairs. Table 10 shows the EIS fitting results of the three material pairs using ZSimpWin software. It could be seen that the R_{film} value of the sample after rubbing with 316 L was the largest, the sample after rubbing with Al_2O_3 was the smallest, and the sample after rubbing with CoCrMo was in the middle. Therefore, the samples with a thick material transfer layer had a better corrosion resistance. This illustrated the fact that the material transfer layer formed on the surface of the material played a protective role under the 316 L/Ti6Al4V and CoCrMo/Ti6Al4V pairs.

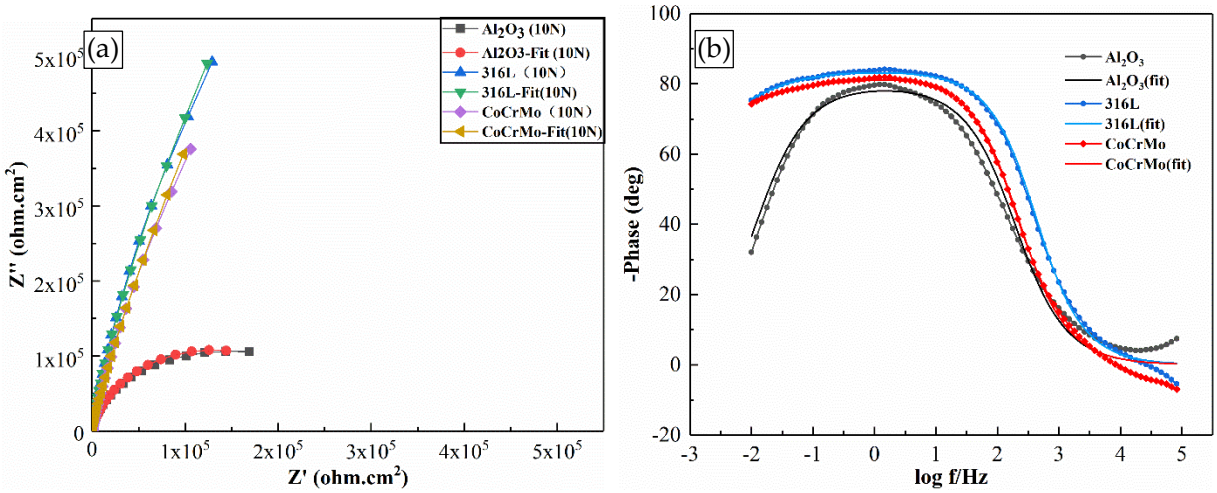

Figure 10. The electrochemical impedance spectroscopy (EIS) of three types of matching pairs under the same load. (**a**) Nyquist diagram; (**b**) Bode diagram.

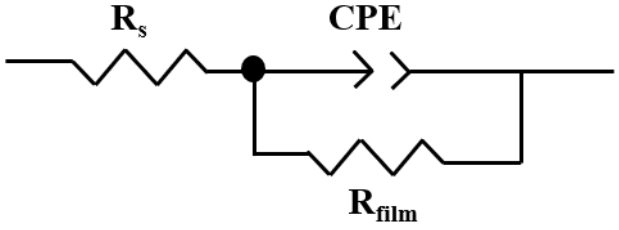

Figure 11. Equivalent circuit model of the impedance spectrum.

Table 10. The fitting results of EIS under three material pairs.

	Rs ($\Omega \cdot cm^{-2}$)	CPE ($F \cdot cm^{-2}$)	n	R_{film} (Ω)
Al_2O_3/Ti6Al4V	47.85 ± 0.51	$3.895 \times 10^{-5} \pm 9.69 \times 10^{-7}$	0.9	$2.592 \times 10^{4} \pm 76.36$
316 L/Ti6Al4V	27.75 ± 0.17	$2.348 \times 10^{-5} \pm 1.69 \times 10^{-6}$	0.8	$1.504 \times 10^{6} \pm 1484.92$
CoCrMo/Ti6Al4V	46.78 ± 0.43	$2.792 \times 10^{-5} \pm 1.62 \times 10^{-6}$	0.9	$1.605 \times 10^{5} \pm 989.95$

3.5. Limitations

This research, however, was subject to several limitations. First, in clinical application, the load range of the joint interface is very large, and this study only considered the fretting corrosion behaviours under some conditions. Additionally, no efforts were made to determine the contribution of wear and corrosion in the fretting corrosion process and their interaction. Only the worn surface of Ti6Al4V was characterized, but that of the friction pair was not characterized. It would be more sensible to combine the damage situation of the two to determine which material pair is the best. Longer time tests and joint motion simulation tests in vitro should be conducted to determine which pair is preferable.

4. Conclusions

The fretting-corrosion performances of three typical material pairs for modular head-neck junctions in hip implants were investigated and compared, and the following conclusions were drawn:

(a) Within the given load range, the fretting regime of Al_2O_3/Ti6Al4V and 316 L/Ti6Al4V pairs changed from SR to MFR as the load increased, while the CoCrMo/Ti6Al4V pair was always in SR, indicating that the CoCrMo/Ti6Al4V pair was easier to slip.

(b) For the Al_2O_3/Ti6Al4V pair, the damage mechanism was mainly abrasive wear and corrosive wear, while for the 316 L/Ti6Al4V and CoCrMo/Ti6Al4V pairs, a layer of material transfer layer was formed on the worn surface, and the wear mechanism was mainly adhesive wear and corrosive wear with slight abrasive wear.

(c) Judging from the wear morphology, the damage to the Ti6Al4V alloy was the smallest when paired with Al_2O_3, while it was more serious when paired with 316 L and CoCrMo.

(d) The electrochemical impedance spectrum results show that the material transfer layer formed on the surface of the material can protect the material from corrosion under the 316 L/Ti6Al4V and CoCrMo/Ti6Al4V pairs.

Author Contributions: Conceptualization, Z.J.; methodology, X.Z.; software, D.W.; validation, J.P.; formal analysis, J.P.; investigation, D.W. and J.P.; resources, Z.J.; data curation, D.W. and J.P.; writing—original draft preparation, D.W. and J.P.; writing—review and editing, Y.Z. and X.Z.; visualization, D.W. and J.P.; supervision, Z.J., Y.Z., and X.Z.; project administration, Z.J., Y.Z., and X.Z.; funding acquisition, Z.J. and Y.Z. All authors have read and agreed to the published version of the manuscript.

Funding: This research was funded by the National Natural Science Foundation of China, grant number 51775460, and the Science and Technology Planning Project of Sichuan province, grant number 2020YJ0032.

Institutional Review Board Statement: "Not applicable" for studies not involving humans or animals.

Informed Consent Statement: "Not applicable" for studies not involving humans.

Data Availability Statement: Data is contained within the article.

Conflicts of Interest: The authors declare no conflict of interest.

References

1. Zhang, L.; Haddouti, E.-M.; Welle, K.; Burger, C.; Kabir, K.; Schildberg, F.A. Local Cellular Responses to Metallic and Ceramic Nanoparticles from Orthopedic Joint Arthroplasty Implants. *Int. J. Nanomed.* **2020**, *15*, 6705–6720. [CrossRef] [PubMed]
2. Dos Santos, C.T.; Barbosa, C.; Monteiro, M.J.; Abud, I.C.; Caminha, I.M.V.; Roesler, C.R.M. Characterization of the fretting corrosion behavior, surface and debris from head-taper interface of two different modular hip prostheses. *J. Mech. Behav. Biomed. Mater.* **2016**, *62*, 71–82. [CrossRef] [PubMed]
3. McTighe, T.; Brazil, D.; Keppler, L.; Keggi, J.; McPherson, E. Metallic Modular Taper Junctions in Total Hip Arthroplasty. *Reconstr. Rev.* **2015**, *5*, 29–42. [CrossRef]
4. Cooper, H.J.; Urban, R.M.; Wixson, R.L.; Meneghini, R.M.; Jacobs, J.J. Adverse Local Tissue Reaction Arising from Corrosion at the Femoral Neck-Body Junction in a Dual-Taper Stem with a Cobalt-Chromium Modular Neck. *J. Bone Jt. Surg. Am.* **2013**, *95*, 865–872. [CrossRef] [PubMed]
5. Farhoudi, H.; Fallahnezhad, K.; Oskouei, R.H.; Taylor, M. A finite element study on the mechanical response of the head-neck interface of hip implants under realistic forces and moments of daily activities: Part 1, level walking. *J. Mech. Behav. Biomed. Mater.* **2017**, *75*, 470–476. [CrossRef] [PubMed]
6. Fallahnezhad, K.; Farhoudi, H.; Oskouei, R.H.; Taylor, M. A finite element study on the mechanical response of the head-neck interface of hip implants under realistic forces and moments of daily activities: Part 2. *J. Mech. Behav. Biomed. Mater.* **2018**, *77*, 164–170. [CrossRef]
7. Ponthiaux, P.; Wenger, F.; Drees, D.; Celis, J.P. Electrochemical techniques for studying tribocorrosion processes. *Wear* **2004**, *256*, 459–468. [CrossRef]
8. Ding, H.; Zhou, G.; Dai, Z.; Bu, Y.; Jiang, T. Corrosion wear behaviors of 2024Al in artificial rainwater and seawater at fretting contact. *Wear* **2009**, *267*, 292–298. [CrossRef]
9. Salasi, M.; Stachowiak, G.B.; Stachowiak, G.W. New Experimental Rig to Investigate Abrasive–Corrosive Characteristics of Metals in Aqueous Media. *Tribol. Lett.* **2010**, *40*, 71–84. [CrossRef]
10. Sivakumar, B.; Kumar, S.; Sankara Narayanan, T.S.N. Fretting corrosion behaviour of Ti–6Al–4V alloy in artificial saliva containing varying concentrations of fluoride ions. *Wear* **2011**, *270*, 317–324. [CrossRef]
11. Dyrkacz, R.M.R.; Brandt, J.-M.; Ojo, O.A.; Turgeon, T.R.; Wyss, U.P. The Influence of Head Size on Corrosion and Fretting Behaviour at the Head-Neck Interface of Artificial Hip Joints. *J. Arthroplast.* **2013**, *28*, 1036–1040. [CrossRef] [PubMed]
12. Panagiotidou, A.; Meswania, J.; Hua, J.; Muirhead-Allwood, S.; Hart, A.; Blunn, G. Enhanced wear and corrosion in modular tapers in total hip replacement is associated with the contact area and surface topography. *J. Orthop. Res.* **2013**, *31*, 2032–2039. [CrossRef] [PubMed]
13. Kao, Y.Y.J.; Koch, C.N.; Wright, T.M.; Padgett, D.E. Flexural Rigidity, Taper Angle, and Contact Length Affect Fretting of the Femoral Stem Trunnion in Total Hip Arthroplasty. *J. Arthroplast.* **2016**, *31*, S254–S258. [CrossRef] [PubMed]
14. Jauch, S.Y.; Huber, G.; Sellenschloh, K.; Haschke, H.; Baxmann, M.; Grupp, T.M.; Morlock, M.M. Micromotions at the taper interface between stem and neck adapter of a bimodular hip prosthesis during activities of daily living. *J. Orthop. Res.* **2013**, *31*, 1165–1171. [CrossRef]
15. Mann, M.A.; Tanzer, D.; Tanzer, M. Severe metal-induced osteolysis many years after unipolar hip endoprosthesis. *Clin. Orthop. Relat. Res.* **2013**, *471*, 2078–2082. [CrossRef] [PubMed]
16. Svensson, O.; Mathiesen, E.B.; Reinholt, F.; Blomgren, G.J.J. Formation of a fulminant soft-tissue pseudotumor after uncemented hip arthroplasty. A case report. *JBJS* **1988**, *70*, 1238–1242. [CrossRef]
17. Collier, J.P.; Surprenant, V.A.; Jensen, R.E.; Mayor, M.B.; Surprenant, H.P. Corrosion between the components of modular femoral hip prostheses. *J. Bone Jt. Surg. Br.* **1992**, *74*, 511–517. [CrossRef]
18. Geringer, J.; Fridrici, V.; Ding, H.; Kim, K.; Taylor, T.; Semetse, L.; Ehsani-Majd, S.; Olubambi, P.; Fontaine, J.; Kapsa, P. Some Hard or Soft Coatings to Protect the Pristine Biometallic Substrates under Fretting-Corrosion Solicitations: What Should Be the Best Solution? *Lubricants* **2020**, *8*, 55. [CrossRef]
19. Rasool, G.; El Shafei, Y.; Stack, M.M. Mapping Tribo-Corrosion Behaviour of TI-6AL-4V Eli in Laboratory Simulated Hip Joint Environments. *Lubricants* **2020**, *8*, 69. [CrossRef]
20. Sadiq, K.; Sim, M.A.; Black, R.A.; Stack, M.M. Mapping the Micro-Abrasion Mechanisms of CoCrMo: Some Thoughts on Varying Ceramic Counterface Diameter on Transition Boundaries In Vitro. *Lubricants* **2020**, *8*, 71. [CrossRef]
21. Brayda-Bruno, M.; Fini, M.; Pierini, G.; Giavaresi, G.; Rocca, M.; Giardino, R. Evaluation of Systemic Metal Diffusion after Spinal Pedicular Fixation with Titanium Alloy and Stainless Steel System: A 36-month Experimental Study in Sheep. *Int. J. Artif. Organs* **2018**, *24*, 41–49. [CrossRef]
22. Kumar, S.; Sivakumar, B.; Sankara Narayanan, T.S.N.; Ganesh Sundara Raman, S.; Seshadri, S.K. Fretting-corrosion mapping of CP-Ti in Ringer's solution. *Wear* **2010**, *268*, 1537–1541. [CrossRef]
23. Eckert, J.A.; Mueller, U.; Jaeger, S.; Panzram, B.; Kretzer, J.P. Fretting and Corrosion in Modular Shoulder Arthroplasty: A Retrieval Analysis. *BioMed Res. Int.* **2016**, *2016*, 1695906. [CrossRef] [PubMed]
24. Teeter, M.G.; Carroll, M.J.; Walch, G.; Athwal, G.S. Tribocorrosion in shoulder arthroplasty humeral component retrievals. *J. Shoulder Elb. Surg.* **2016**, *25*, 311–315. [CrossRef] [PubMed]
25. Lukina, E.; Kollerov, M.; Meswania, J.; Khon, A.; Panin, P.; Blunn, G.W. Fretting corrosion behavior of nitinol spinal rods in conjunction with titanium pedicle screws. *Mater. Sci. Eng. C Mater. Biol. Appl.* **2017**, *72*, 601–610. [CrossRef]

26. Mali, S.A.; Singh, V.; Gilbert, J.L. Effect of mixed alloy combinations on fretting corrosion performance of spinal screw and rod implants. *J. Biomed. Mater. Res. B Appl. Biomater.* **2017**, *105*, 1169–1177. [CrossRef]
27. Kang, Y.-K.; Kim, M.-H.; Kim, J.-W.; Tien, T.N.; Lim, D.-H.; Chun, H.-J. Analysis on Wear Phenomenon of Artificial Knee Joint Based on FEM and Mechanical Test. *Int. J. Precis. Eng. Manuf.* **2018**, *19*, 1211–1217. [CrossRef]
28. Swaminathan, V.; Gilbert, J.L. Fretting corrosion of CoCrMo and Ti6Al4V interfaces. *Biomaterials* **2012**, *33*, 5487–5503. [CrossRef]
29. Royhman, D.; Patel, M.; Runa, M.J.; Jacobs, J.J.; Hallab, N.J.; Wimmer, M.A.; Mathew, M.T. Fretting-corrosion in hip implant modular junctions: New experimental set-up and initial outcome. *Tribol. Int.* **2015**, *91*, 235–245. [CrossRef]
30. Barril, S.; Debaud, N.; Mischler, S.; Landolt, D. A tribo-electrochemical apparatus for in vitro investigation of fretting–corrosion of metallic implant materials. *Wear* **2002**, *252*, 744–754. [CrossRef]
31. Barril, S.; Mischler, S.; Landolt, D. Influence of fretting regimes on the tribocorrosion behaviour of Ti6Al4V in 0.9wt.% sodium chloride solution. *Wear* **2004**, *256*, 963–972. [CrossRef]
32. Royhman, D.; Patel, M.; Runa, M.J.; Wimmer, M.A.; Jacobs, J.J.; Hallab, N.J.; Mathew, M.T. Fretting-corrosion behavior in hip implant modular junctions: The influence of friction energy and pH variation. *J. Mech. Behav. Biomed. Mater.* **2016**, *62*, 570–587. [CrossRef]
33. Royhman, D.; Patel, M.; Jacobs, J.J.; Wimmer, M.A.; Hallab, N.J.; Mathew, M.T. In vitro simulation of fretting-corrosion in hip implant modular junctions: The influence of pH. *Med. Eng. Phys.* **2018**, *52*, 1–9. [CrossRef] [PubMed]
34. Liu, Y.P.; Gilbert, J.L. The effect of simulated inflammatory conditions and pH on fretting corrosion of CoCrMo alloy surfaces. *Wear* **2017**, *390–391*, 302–311. [CrossRef]
35. Wang, S.; Zhang, D.; Hu, N.; Zhang, J. Effect of angular displacement amplitude on the torsional fretting corrosion behavior of CoCrMo alloy in different synovial fluid. *RSC Adv.* **2016**, *6*, 66087–66097. [CrossRef]
36. Wang, S. Torsional Fretting Corrosion Behaviors of the CoCrMo/Ti6Al4V Couple. *Int. J. Electrochem. Sci.* **2018**, 6414–6425. [CrossRef]
37. Lin, X.-Z.; Zhu, M.-H.; Cai, Z.-B.; Dou, B.-J.; Cui, X.-J. Torsional fretting corrosion behaviours of Ti6Al4V alloys in Hank's simulated body fluid. *Corros. Eng. Sci. Technol.* **2019**, *54*, 298–309. [CrossRef]
38. Liu, D.; Wang, Q.; Zhang, D.; Wang, J.; Zhang, X. Torsional Friction Behavior of Contact Interface between PEEK and CoCrMo in Calf Serum. *J. Tribol.* **2019**, *141*, 011602. [CrossRef]
39. Gilbert, J.L.; Buckley, C.A.; Jacobs, J.J. In-Vivo Corrosion of Modular Hip-Prosthesis Components in Mixed and Similar Metal Combinations—The Effect of Crevice, Stress, Motion, and Alloy Coupling. *J. Biomed. Mater. Res.* **1993**, *27*, 1533–1544. [CrossRef]
40. Mathiesen, E.B.; Lindgren, J.U.; Blomgren, G.G.A.; Reinholt, F.P. Corrosion of Modular Hip Prostheses. *J. Bone Jt. Surg. Br.* **1991**, *73*, 569–575. [CrossRef]
41. Fouvry, S.; Liskiewicz, T.; Kapsa, P.; Hannel, S.; Sauger, E. An energy description of wear mechanisms and its applications to oscillating sliding contacts. *Wear* **2003**, *255*, 287–298. [CrossRef]
42. Chaudhry, V.; Kailas, S.V. Fretting studies on self-mated stainless steel and chromium carbide coated surfaces under controlled environment conditions. *Wear* **2013**, *301*, 524–539. [CrossRef]